ChemSusChem

Research Article
doi.org/10.1002/cssc.202400948

Chemistry Europe
European Chemical Societies Publishing

www.chemsuschem.org

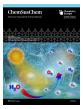

Graphitic Carbon Nitride Structures on Carbon Cloth Containing Ultra- and Nano-Dispersed NiO for Photoactivated Oxygen Evolution

Enrico Scattolin,[a] Mattia Benedet,[a, b] Gian Andrea Rizzi,[a, b] Alberto Gasparotto,[a, b] Oleg I. Lebedev,[c] Davide Barreca,*[b] and Chiara Maccato[a, b]

The development of low-cost and high-efficiency oxygen evolution reaction (OER) photoelectrocatalysts is a key requirement for H_2 generation *via* solar-assisted water splitting. In this study, we report on an amenable fabrication route to carbon cloth-supported graphitic carbon nitride (gCN) nanoarchitectures, featuring a modular dispersion of NiO as co-catalyst. The synergistic interaction between gCN and NiO, along with the tailoring of their size and spatial distribution, yield very attractive OER performances and durability in freshwater splitting, of great significance for practical end-uses. The potential of gCN electrocatalysts containing ultra-dispersed, *i.e.* "quasi-atomic" NiO, exhibiting a higher activity than the ones containing nickel oxide nanoaggregates, is further highlighted by their activity even in real seawater. This work suggests that efficient OER catalysts can be designed through the construction of optimized interfaces between transition metal oxides and carbon nitride, yielding inexpensive and promising noble metal-free systems for real-world applications.

Introduction

Over the last two decades, the global population growth and the fast industrial development have produced an ever increasing demand of clean and renewable energy, triggered by the extensive use of depleting fossil fuels and the resulting severe consequences on environment, human health and climate changes.[1] In this regard, since 2017 the International Hydrogen Commission has been advocating the importance of molecular hydrogen (H_2) as a strategic energy vector to address the global energy crisis, thanks to its perfect recyclability, clean burning process, and high energy density ($\approx$145 kJ×g^{-1}).[1a,b,f,2] These features are in line with the "Net Zero by 2050" report from the International Energy Agency (IEA), stating that massive deployment of clean and efficient energy technologies must achieve net zero CO_2 emissions by 2050, limiting the global temperature increase to 1.5 °C, as targeted in the Paris Agreement.[3]

The development of a global hydrogen economy can be accelerated only by providing a renewable and sustainable green H_2 supply, that can be successfully achieved through electrochemical water splitting, possibly activated by solar illumination.[1b,f,4] Nevertheless, electrochemical water splitting accounts so far for only 3–5 % of industrial H_2 production, due to the sluggish oxygen evolution reaction (OER), an energetically uphill process associated with a high overpotential.[1a,b,2a,4d,h,5] As a consequence, the key to establishing industrial viability for the related sunlight-to-hydrogen conversion is the engineering of efficient noble-metal free OER photoelectrocatalysts,[5a,6] as alternatives to the benchmark RuO_2 and IrO_2, plagued by high cost, natural scarcity, and limited stability.[1a,b,2b,d,4a,5c,d,g,7]

Among the various OER photoelectrocatalysts developed in recent years,[5g] *n*-type graphitic carbon nitride (gCN), composed of nature-abundant elements, is extremely attractive thanks to the green character, low cost, thermal/chemical stability, optical properties and tunable electronic structure.[1c–e,4b,e,8] Against these advantages, gCN suffers from a low specific surface area and a modest activity, related to the high recombination rate of photogenerated electrons and holes.[1f,i,4a,7–8,9] Among the various research efforts devoted to bypassing such shortcomings,[1h,9c] morphological control and the construction of heterojunctions between gCN and nano-sized transition metals/oxides stand as valuable means to improve charge carrier kinetics, positively affecting the ultimate functional performances.[1b,d,2c,5e,7,8d,f,g,9a,b,10]

Among transition metal-based materials, Ni-containing ones exhibit a favorable activity, strongly dependent on their actual structure and morphology.[1g,i,4f,h,5a,h,6b,8e,11] In particular, low-cost *p*-type nanostructured nickel(II) oxide, endowed with earth abundance, and chemical stability,[1d,e,3,4b,8f,12] features an attractive reactivity[1b,7,9b,13] dependent also on the used

[a] *Department of Chemical Sciences, Padova University and INSTM, Padova, Italy*
[b] *CNR-ICMATE and INSTM, Department of Chemical Sciences, Padova University, Padova, Italy*
[c] *Laboratoire CRISMAT, UMR 6508 Normandie Université, CNRS, ENSICAEN, UNICAEN, Caen, Cedex 4, France*

Correspondence: *Dr. Davide Barreca, CNR-ICMATE and INSTM, Department of Chemical Sciences,, Padova University,, Via Marzolo 1, 35131 Padova, Italy.*
Email: davide.barreca@unipd.it

Supporting information for this article is available on the WWW under https://doi.org/10.1002/cssc.202400948

support backbone, that could modulate its dispersion facilitating mass transport and electron transfer kinetics.[4a,5a] As a consequence, the combination of a gCN support with NiO to yield composite systems is deemed to increase electrochemically active sites, resulting in an enhanced OER activity thanks to the synergistical NiO/gCN interaction.[4b,5a,c] Additional degrees of freedom to boost the composite performances are offered by the control of both NiO loading and its ultra- *vs.* nano-dispersion, through a suitable choice of the preparation route and processing conditions.[1i,11d] Recently, the construction of ultra-[14] and atomically dispersed[2e,4f,g] Ni- (but also Cu- and Pt-) based active sites in carbon nitride has been demonstrated to promote charge transfer and speed up surface reactions, providing very attractive performances.[9a,15] The incorporation of highly dispersed Ni-containing nanoaggregates during the polymerization process could finely regulate the resulting gCN structures, promoting thus the obtainment of an engineered band energetics for improved light absorption, and effective catalytic reactions.[5b,9a]

So far, water splitting (photo)electrocatalysts based on NiO and gCN have been used both as cathodes[1h,i,4e,7,8c,11c] and as anodes[1b,2a,4f–h,5a,c,6a,7] for the hydrogen evolution reaction (HER) and the OER, respectively. Up to date, similar systems have been prepared both from powders eventually mixed with binders/conductive species,[1h,2b,5a,c,6a,7,8f,14] and as nanostructures/thin films directly grown onto suitable supports.[2a,3,4b,e,f,11b] The latter materials, featuring an intimate material-substrate contact, represent a preferred choice for eventual real-world end-uses, to overcome undesired aggregation/phase segregation and improve the catalyst conductivity and durability.[4f]

In the present study, we develop supported gCN modified with NiO as co-catalyst by a fast and facile electrophoretic deposition (EPD) route, a valuable and flexible strategy for the fabrication and processing of nanoscale materials.[8h,9c,10a] The target systems are deposited on flexible carbon cloth (CC) substrates featuring a large surface area, high electronic conductivity, good corrosion resistance, and favorable interactions with gCN. CC-supported active materials can be directly used as electrodes without the need of introducing polymeric binders or conductive additives,[16] and offer important advantages in terms of catalyst stability and recyclability.[8k,11a] Particular attention is dedicated to examining the interplay between the nano- *vs.* ultra-dispersion of NiO in the hosting gCN (ultra-dispersion hereafter referring to a NiO "quasi-atomic" distribution), and the resulting chemico-physical and functional characteristics in photoassisted OER. The results of a multi-technique characterization and of functional electrochemical tests indicate that the dispersion degree of nickel(II) oxide has a significant influence on material behavior. In particular, for ultra-dispersed NiO-loaded gCN, the OER activity increment turned out to be the highest in comparison to the pristine gCN, with a photocurrent density of 3.24 mA/cm^2 at 1.65 V *vs.* the reversible hydrogen electrode (RHE) and a Tafel slope of 86 mV/dec. These features open important perspectives toward the sustainable conversion of solar light into chemical energy.[17] The system applicative potential is further highlighted by their functional behavior in seawater, an appealing alternative to conventional freshwater for large-scale H_2 production thanks to the almost unlimited reservoirs and easy combination with large-scale offshore renewable energy.[2a,d,4a,5d,13c]

Results and Discussion

Figure 1 reports a schematic representation of the preparation route adopted in the present work. The synthesis of gCN-NiO powders was performed by mixing carbon nitride obtained from cyanuric acid and melamine supramolecular adduct[10a] with different amounts of nickel(II) acetate, as precursors. Particular attention was devoted to investigating the influence of NiO dispersion into the carbon nitride matrix for the improvement of charge carrier separation, one of carbon nitride's major drawbacks. Fabrication of electrode materials was carried out through EPD under suitably optimized con-

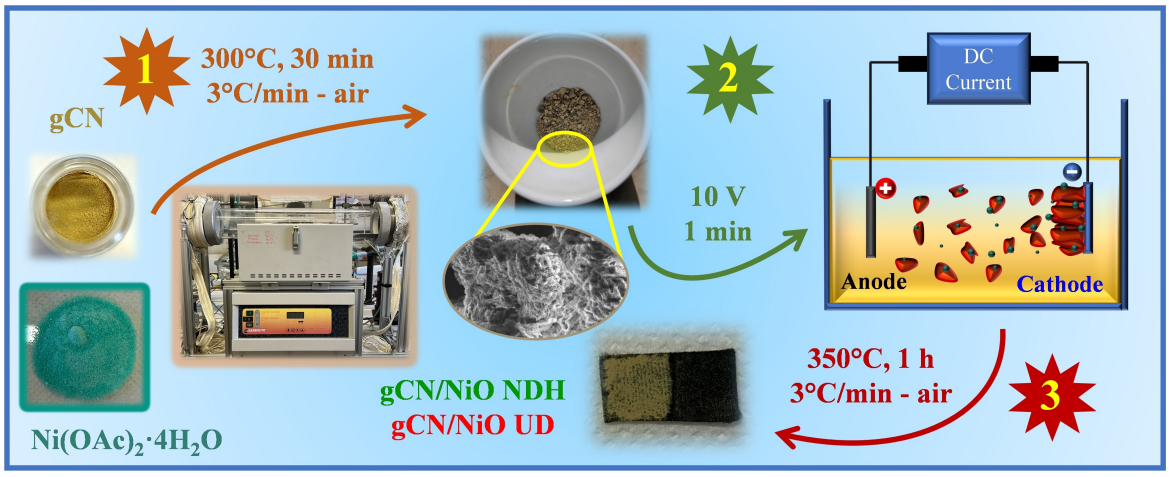

Figure 1. Sketch of the multi-step procedure adopted in the present study for the fabrication of graphitic carbon nitride (gCN)-based electrocatalysts functionalized with ultra- and nano-dispersed NiO (gCN/NiO UD and gCN/NiO NDH, respectively): 1) preparation of precursor powders; 2) electrophoretic deposition on carbon cloth substrates; 3) *ex situ* thermal treatment.

ditions, that enabled to obtain homogeneous deposits featuring a good adhesion to the underlying CC substrate. Hereafter, samples are named as gCN/NiO UD (ultra-dispersed) and gCN/NiO NDH (nano-dispersed-high). For comparison, a third kind of specimens, gCN/NiO NDL (nano-dispersed-low) was also fabricated and characterized. For specimens gCN/NiO NDH and gCN/NiO NDL, "high" and "low" refer, respectively, to a NiO loading higher or lower than gCN/NiO UD (see the Electronic Supporting Information).

Material Chemico-Physical Characterization

In the present work, particular efforts were devoted to the system chemico-physical investigation by means of complementary analytical techniques. Preliminary X-ray diffraction (XRD) measurements on bare gCN and gCN/NiO UD powders (see Figure S1), revealed that carbon nitride structural features were unaffected by nickel oxide introduction. Similar conclusions were ascertained for gCN/NiO NDH and gCN/NiO NDL powders. The corresponding CC-supported samples were then subjected to a thorough structural, optical and compositional characterization. Figure 2a displays representative Fourier transform infrared (FT-IR) spectra for bare gCN, gCN/NiO NDH and gCN/NiO UD deposits, confirming the obtainment of a polymeric graphitic carbon nitride structure. In particular, the peak at 814 cm^{-1} was ascribed to the breathing modes of triazine units,[10b] the one at ≈891 cm^{-1} to the wagging mode of primary and secondary amino groups,[18] the signals between 1200 and 1700 cm^{-1} to stretching modes of C–N heterocycles,[10b] and the ones in the 3000–3500 cm^{-1} range to the stretching of amino ($-NH_x$, x = 1,2) groups.[19] The presence of the latter moieties, that should not be present in an ideal gCN structure, was deemed to favourably improve the specimen photoelectrochemical activity,[10a] as demonstrated by functional results (see below).

Since the system optical properties are of great importance for the target application, optical absorption analyses were performed (Figures 2b and S2a). As can be observed, the recorded spectra were dominated by a pronounced absorption edge at λ < 450 nm, associated to the carbon nitride interband transition. The functionalized specimens showed an enhanced light harvesting with respect to bare gCN, the highest absorption corresponding to sample gCN/NiO UD. The optical

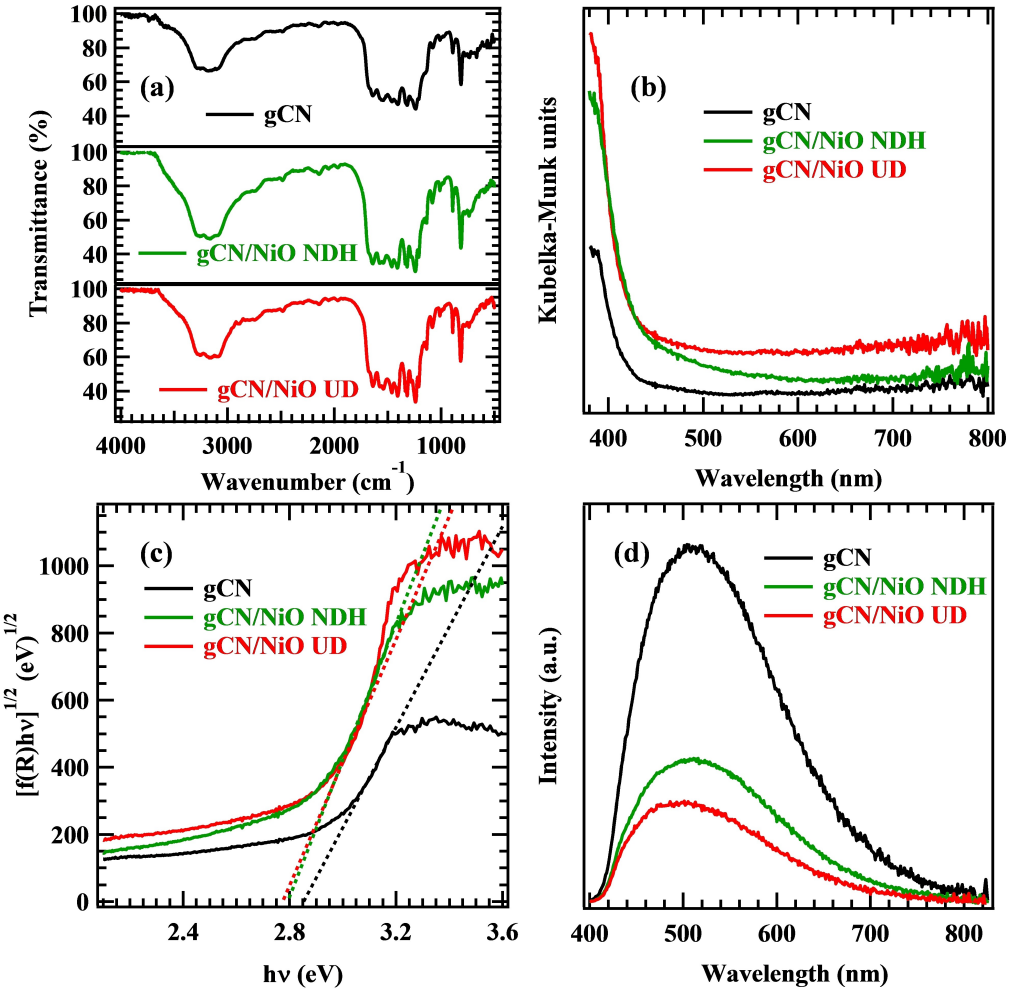

Figure 2. FT-IR (a) and optical spectra (b) of gCN-based electrocatalysts functionalized with ultra- and nano-dispersed NiO. The corresponding Tauc plots and photoluminescence (PL) spectra are displayed in panels (c) and (d), respectively.

bandgaps (E_G), extrapolated from Tauc plots (Figures 2c and S2b), were very similar for all deposits, suggesting that no carbon nitride doping, with consequent creation of impurity levels in the band gap, took place under the adopted conditions.[2c] The average E_G (2.82 eV) was higher than those reported in the literature,[2c,10a,b] a phenomenon likely due to the occurrence of quantum confinement effects[10a] (see also morphological and structural data below).

The recorded PL spectra (Figures 2d and S2c) were characterized by a net emission band centred at $\lambda \approx 510$ nm, attributable to the π^* conduction band→nitrogen lone pair electronic transition, and to a minor contribution at 435 nm, associated to the δ^* conduction band→carbon nitride lone pair transition.[20] In the case of gCN/NiO UD, a blue shift of the band position (≈15 nm) with respect to the other materials was observed and related to a more favourable interaction between the system components,[21] (see below). An analysis of peak intensity suggests an enhanced charge separation according to the order gCN < gCN/NiO NDH < gCN/NiO UD, that will indeed be confirmed by the electrochemical results discussed below.

Important insights into material chemical composition were provided by XPS (see also Figures S3 and S4). Figure 3 reports the high-resolution spectra for gCN/NiO UD. The C1s signal (Figure 3a; see also Figure S5 and Table S1) was deconvoluted by five different components. C_0 was due to both adventitious carbon and C–C bonds in the CC substrate, whereas C_1 was assigned to C-NH_x (x = 1, 2) groups on heptazine ring edges in gCN structure.[2c,5d,10c,13b] For NiO-containing systems, this component was also ascribed to the presence of C–O bonds[1c,d,i,8d] between carbon nitride and nickel(II) oxide, a feature responsible for the direct electronic interplay between the system constituents, resulting in improved OER performances. The predominant band, C_2, was due to carbon atoms in N-C=N groups[2c,5e,8e,f,h,10b,c,16b] and also to a contribution from carbonyl groups of the carbon cloth.[22] Component C_3, ascribed to carboxylate/ester groups due to air exposure of the carbon cloth,[22] confirmed an incomplete coverage of the latter, in line with morphological analyses (see below); finally, band C_4 was related to π-electrons excitation.[8d,23] Since -NH_x groups should not be present in an ideal gCN structure, the obtained data suggest an incomplete precursor condensation during gCN formation. As anticipated, defects arising from the presence of -NH_x species may act as capturing sites, reducing detrimental electron-hole recombination and positively influencing the system photoactivity.[10a,24] In addition, these groups can favour NiO anchoring to gCN, improving thus material stability, and NiO/gCN charge transfer phenomena.[5d] As can be observed in Table S1, upon passing from bare gCN to functionalized samples, components C_1, C_2 and C_4 underwent a BE decrease. This phenomenon suggested the occurrence of interfacial electron transfer from NiO to gCN,[8b] consistent with the formation of *p-n* NiO/gCN heterojunctions[1d,e,8e,f,12] (see also below). The BEs of the mentioned components followed the sequence gCN > gCN/NiO NDL > gCN/NiO NDH > gCN/NiO UD, with the higher variation taking place for the latter specimen. This trend, suggesting a parallel enhancement in the NiO→gCN electron transfer, was also confirmed by a detailed analysis of N1s photopeaks, that resulted from four concomitant contributions (Figures 3b, S6 and Table S2): N_0, the predominant one, ascribed to bi-coordinated N atoms [C=N–C]; N_1, attributed to tri-coordinated N centres in gCN lattice [N–$(C)_3$]; N_2, due to uncondensed ammino groups; N_3, related to π-electrons excitation.[1c,e,8b–d,h,10a,13b] In accordance with the C1s case, even the BEs of N1s components underwent a downward shift according to the aforementioned order, corroborating thus the presence of an electronic interplay between gCN and NiO,[5a] more efficient for gCN/NiO UD. Ni2p signals (Figure 3c and S7) were characterized by a multiplet structure, with intense satellites located at BEs ≈6 eV higher than the corresponding j = 3/2 and j = 1/2 components (see the Supporting Information, page S13 for a detailed description). For bare NiO (Figure S7c), both the shape and the energy position are in line with those expected for Ni(II) in bulk NiO.[25] The absence of signals at 853.2 eV and 852.7 eV allowed to rule out the presence of Ni(0) and Ni nitride in appreciable amounts.[5c,7,8e,9a] If compared to the bare NiO reference sample, the BEs of Ni2p components were shifted to higher BE values according to the sequence gCN/NiO UD < gCN/NiO NDL < gCN/NiO NDH (Table S3). This phenomenon is apparently in contrast with the above observations, that would suggest the highest Ni2p BEs for gCN/NiO UD.

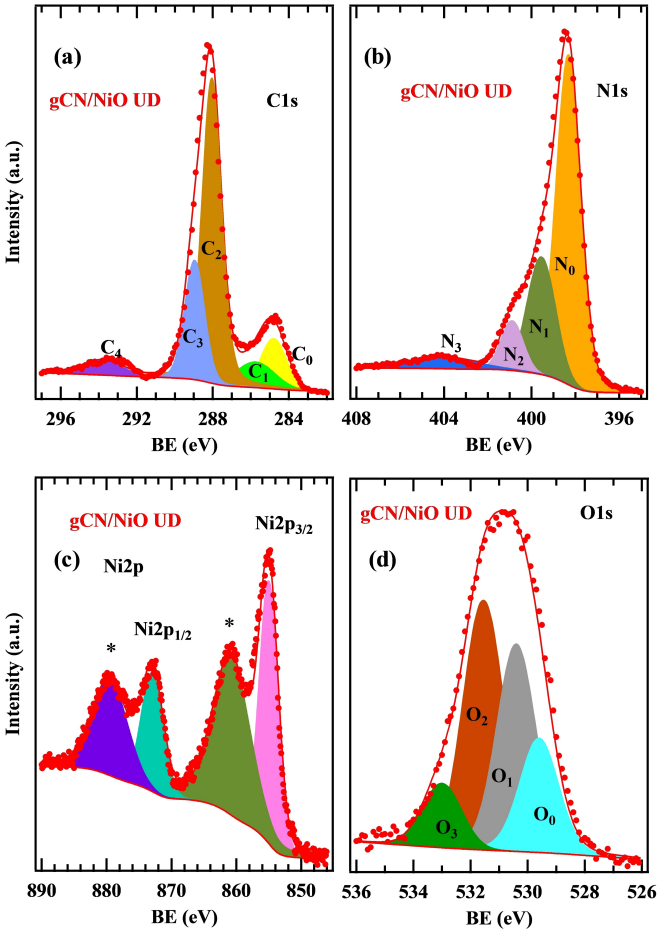

Figure 3. High-resolution XPS core level spectra for C 1s (a), N 1s (b), Ni 2p (c), and O 1s (b) for a gCN specimen containing ultra-dispersed NiO. Satellite peaks are marked by * in panel (c).

The above results can be explained basing on transmission electron microscopy (TEM) outcomes (see below), that highlight a "quasi-atomic" dispersion of NiO into gCN for the gCN/NiO UD sample. As recently reported in the literature,[9a] for ultra-dispersed NiO-based systems, the oxidation state of Ni centers is lower than the nominal value (II). Therefore, the blue shift in Ni2p BE caused by the mentioned NiO→gCN electron transfer is partially offset, for sample gCN/NiO UD, by the ultra-dispersion evidenced by TEM data.

As concerns O1s signals (Figures 3d and S8; Table S4), three bands could be identified for bare NiO: O_0, due to lattice oxygen in Ni(II) oxide;[1i,4a,8c,13a] O_2, attributed to the presence of hydroxyl groups chemisorbed on surface defects;[7,8f,10a,c,13a] and O_3, ascribed to physisorbed water.[2a,8d,26] For bare gCN, component O_0 was obviously absent. Band O_1 at 530.4 eV, present in all carbon nitride-containing samples, was ascribable to carbonyl groups on the CC substrate.[22] For composite systems, signal O_2 resulted also from the contribution of carboxylate/ester groups,[27] whereas component O_3 contained even the contribution from C–O bonds between carbon nitride and Ni(II) oxide.[1c,i,10a]

In order to investigate the system morphology as a function of the adopted processing conditions, field-emission scanning electron microscopy (FE-SEM) images were collected (Figures 4 and S9). Specimens gCN/NiO UD and gCN/NiO NDH were both characterized by the occurrence of spherical-like carbon nitride aggregates featuring a relatively broad size distribution (1–8 μm), resulting from the assembly of exfoliated sheets. These aggregates homogeneously covered carbon cloth fibers for sample gCN/NiO UD, but presented an evident clustering for specimen gCN/NiO NDH (compare Figures 4a–b). Despite in both cases NiO nanoparticles could be hardly detected, nickel signals were evident in energy dispersive X-ray spectroscopy (EDXS) chemical maps (Figures 4c–d). As can be noticed, C Kα and N Kα signals confirmed that the observed spherical nanoparticles were composed of gCN, whereas Ni Kα and O Kα maps supported the effective gCN functionalization with nickel(II) oxide. As far as the Ni distribution is concerned, in the case of gCN/NiO UD, nickel turned out to be evenly dispersed (Figure 4c, right panel). A similar distribution did not occur for gCN/NiO NDH (Figure 4d, right panel and S10), where aggregation (clustering) phenomena of Ni-containing particles took place. The ultra-dispersion of NiO for specimen gCN/NiO UD may directly boost the corresponding photoelectrochemical performances, increasing the contact area at gCN/NiO interfaces and amount of active sites, ultimately promoting photoproduced electron-hole separation. Conversely, the occurrence of the above-mentioned clustering phenomena for the other systems leads to a reduced content of heterojunctions, resulting in a lower activity.

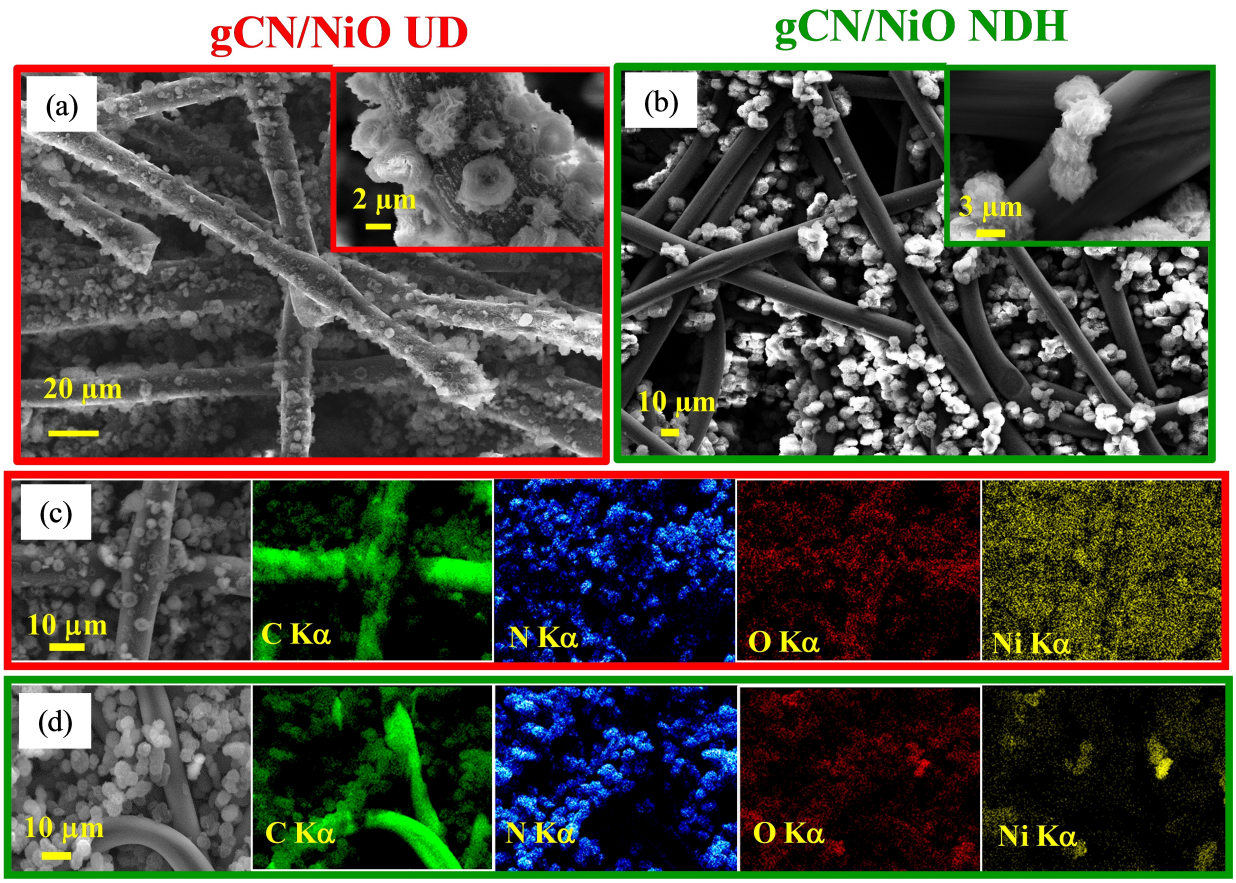

Figure 4. Representative FE-SEM micrographs for (a) gCN/NiO UD, and (b) gCN/NiO NDH electrocatalysts. EDXS elemental maps, recorded on the corresponding electron image, for gCN/NiO UD (c) and gCN/NiO NDH (d).

Since no detailed structural information could be obtained by XRD (see Figure S11), important insights into the system nanostructure, with particular regard to NiO size and spatial distribution as a function of the adopted processing conditions, were obtained by TEM and related techniques. Figure 5 reports representative bright field (BF) high resolution TEM (HRTEM) images and selective area electron diffraction (SAED) pattern for gCN/NiO NDH. The images in Figures 5a–b highlight NiO nanoparticles distributed over the hosting gCN network that, as also revealed by high angle annular dark field-scanning TEM (HAADF-STEM) results (Figures S12a–b), agglomerate into small clusters. The occurrence of cubic NiO [*Fm-3m(225)*; $a=$ 0.418 nm, ICSD 9866) as the sole Ni-containing phase was confirmed by the recorded SAED pattern (Figure 5b, inset), as well as by HRTEM images on NiO nanoparticles collected along [110] and [001] zone axes (Figures 5c–d). For gCN/NiO NDH, analyses in different regions (Figures S12 and S13a–b) evidenced that gCN formed a porous network interpenetrated with low-sized NiO nanoparticles (size range: 2–8 nm; average value: 5 nm). At variance with regions containing the sole gCN (Figure S13c), it is worthwhile noticing the absence of characteristic d_{002} rings for gCN in proximity of NiO (Figure 5b inset), suggesting the presence of amorphous carbon nitride close to nickel(II) oxide. This result can be of interest in view of the target application, since the existence of an amorphous state with abundant defects has been reported to be favorable for electrocatalytic end-uses.[1b] Nonetheless, the intimate gCN/NiO interfacial contact is an important prerequisite in order to favorably benefit from their mutual interplay, ultimately boosting the resulting OER performances in comparison to bare gCN (see below). Functionalized NiO nanoparticles were dispersed in and on the hosting gCN (Figure S12), despite even the occurrence of some gCN agglomerates free from NiO could be observed (Figures S13a–b). STEM-EDXS elemental mapping (Figure S12c; see also Figure S13e) highlighted a homogeneous distribution of carbon and nitrogen within gCN, whose presence was confirmed by TEM/HRTEM and electron diffraction results (Figure S13).

Figure 6 reports representative TEM and STEM-EDXS results for gCN/NiO UD. BF-TEM and HRTEM images in panels a and b show the structure and contrast typically observed for graphitic-like materials. The occurrence of crystalline gCN is confirmed by the SAED pattern in the inset of Figure 6b (ring corresponding to the interplanar spacing $d_{002} \approx 0.32$ nm). Interestingly, no diffraction rings attributable to nickel(II) oxide were present,

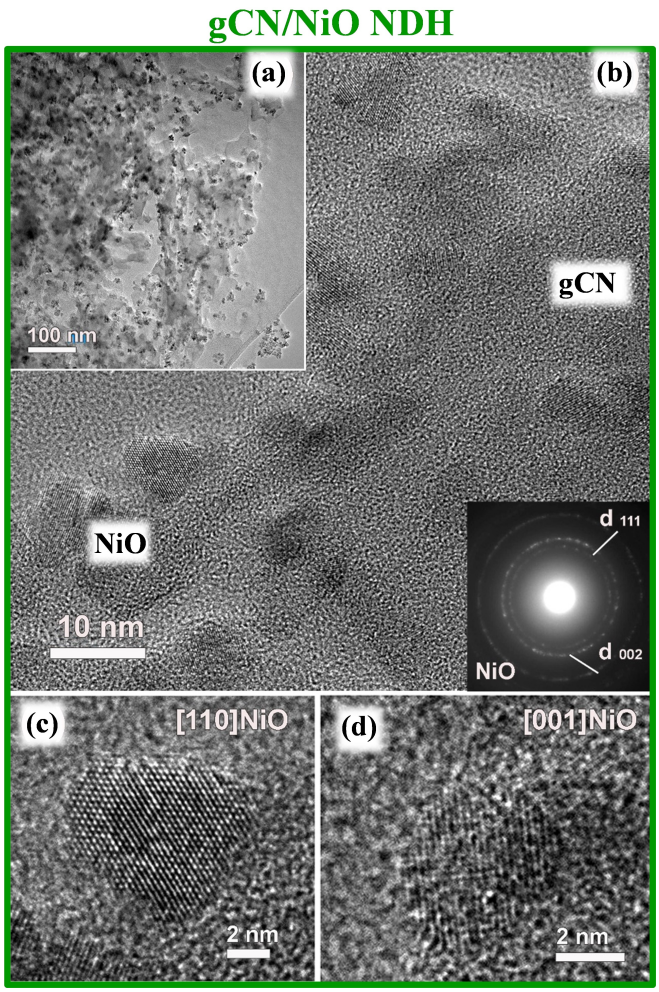

Figure 5. (a) Low magnification BF-TEM image for gCN/NiO NDH; (b) HRTEM image and corresponding SAED pattern, indexed based on NiO cubic structure.[28] (c, d) HRTEM images of selected NiO nanoparticles viewed along [110] and [001] zone axes.

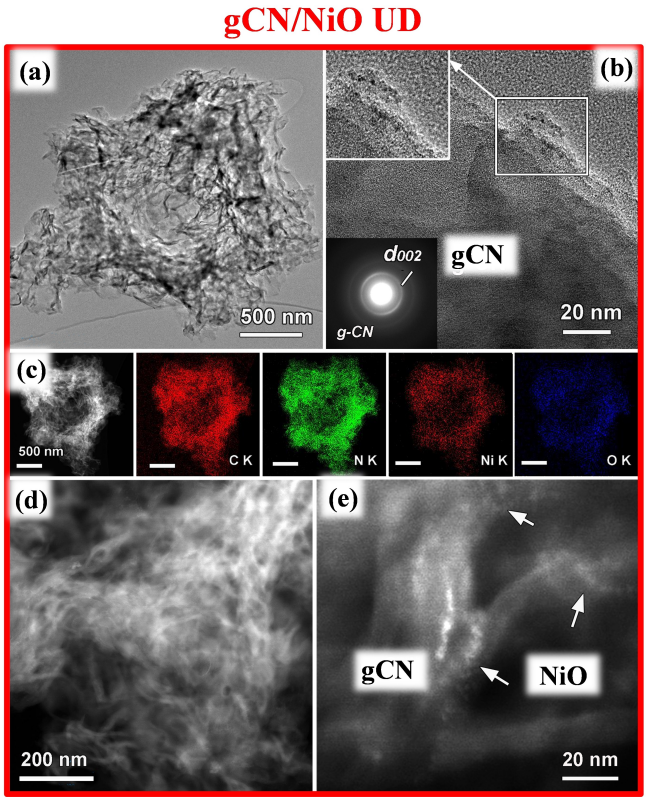

Figure 6. Low magnification BF-TEM (a) and HRTEM (b) images for specimen gCN/NiO UD. In panel (b), a selected area electron diffraction (SAED) pattern is shown as inset. (c) Low magnification HAADF-STEM image and corresponding C K, N K, Ni K and O K EDXS elemental maps. (d) High magnification HAADF-STEM image for the same sample. (e) High resolution HAADF-STEM micrographs of gCN structure decorated by ultra-dispersed NiO, marked by white arrows.

and no NiO-containing nanoparticles could be clearly observed in HRTEM and HAADF-STEM images. Nevertheless, EDXS analyses for gCN/NiO UD (compare Figures 6c and S14b) exhibit well detectable Ni signals even for gCN/NiO UD, highlighting a highly homogeneous nickel distribution throughout the hosting gCN matrix. In particular, EDXS spectra reported in Figure S14 reveal a Ni Kα peak of appreciable intensity for both gCN/NiO NDH and gCN/NiO UD, despite the absence of clearly evident NiO nanoaggregates in HAADF-STEM and HRTEM images for the latter specimen (see Figure 6d). Indeed, a careful inspection of high resolution HAADF-STEM images (Figure 6e) shows that the edges of gCN flakes exhibited an appreciably brighter contrast with respect to the remaining gCN regions, and a careful analysis evidenced the presence of very small, aligned bright dots (whose positions are marked by arrows). Taken together, these results demonstrate that gCN/NiO UD featured the presence of a "quasi-atomic" NiO dispersion, an attractive issue in view of water splitting applications (see below).

Electrochemical Tests

In order to understand if, and up to which extent, the interaction between gCN and NiO nanoparticles affected OER performances, functional tests were carried out in 0.1 M KOH. Figures 7a and S15a display the linear sweep voltammetry (LSV) traces recorded under illumination, that showed a remarkable increase of current density values for all composite samples, both under illumination and in dark conditions (Figure S16), with respect to pristine gCN and NiO (see also Figure S17a). This enhancement was also reflected by the lower Tafel slopes of gCN/NiO composite systems (Figure 7b, S17b-c, and S18), indicating a more favourable reaction kinetics in comparison to bare gCN and NiO electrocatalysts. Such a phenomenon could be traced back to the successful formation of *p-n* NiO/gCN junctions, improving the separation between photogenerated electrons and holes.

The obtained data evidence that the functional performances of composite systems increase according to the trend

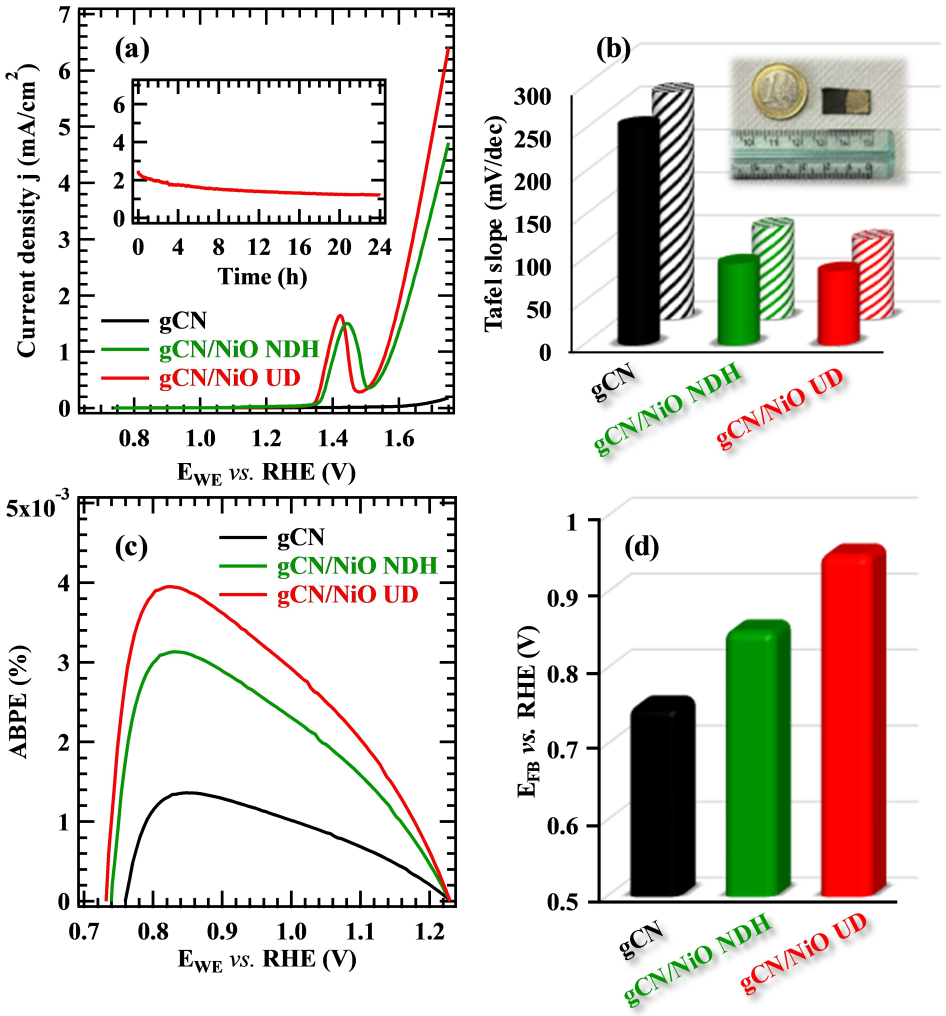

Figure 7. LSV curves recorded under irradiation (a), Tafel slopes under irradiation (solid bars) and in the dark (striped bars) (b), applied bias photon-to-current efficiency (ABPE) % curves (c), and flat band potential values (E_{FB}) (d) for bare gCN, gCN/NiO NDH, and gCN/NiO UD electrocatalysts, obtained in 0.1 M KOH. For gCN/NiO UD, chronoamperometric (CA) measurements at 1.6 V *vs.* RHE and a representative photograph are displayed as insets in panels (a) and (b), respectively. The peak at ≈1.45 V *vs.* RHE in panel (a) is related to the formation of NiOOH during electrochemical testing.[5h,29]

gCN/NiO NDL < gCN/NiO NDH < gCN/NiO UD, the latter yielding the best electrochemical activity. This conclusion was further confirmed by Tafel slopes and ABPE curves (Figures 7c and S15b), showing a beneficial profile shift to lower bias values and a performance step-up upon passing from gCN to gCN/NiO UD. Irrespective of the used electrolyte (KOH or Adriatic alkaline seawater, see also below), the ABPE maxima values obtained in the present study (comprised between 1.2×10^{-3} and 4×10^{-3} %; see Figures 7c and 9b) were higher than those obtained for MnO_2-gCN, gCN-CoO and gCN-$CoFe_2O_4$ photoelectrocatalysts,[2c,10a] and of the same order of magnitude than those of Fe_2O_3-gCN ones functionalized with cobalt phosphate (CoPi).[5d]

How to account for the obtained activity order? Basing on the above discussed characterization data, a possible explanation is related to the amount of NiO in the hosting gCN matrix.[2b,4f,7] For the systems containing nano-dispersed nickel(II) oxide, when the NiO amount is low (gCN/NiO NDL), the interactions among gCN flakes prevail, resulting in their aggregation on the CC surface, as observed in the above presented electron microscopy images. In this case, the NiO/gCN junction plays a minor role and the light effect on the current density is relatively moderate. When the amount of NiO is higher (gCN/NiO NDH), the increased density of NiO/gCN junctions promoting electron-hole separation is responsible for the improved performances. Nevertheless, in this case the aggregation of NiO particles is also observed so that NiO/gCN junctions are not fully accessible to the electrolyte. In a different way, for gCN/NiO UD containing ultra-dispersed nickel(II) oxide, the NiO/gCN interactions are prevailing thanks to the enhanced contact between the system constituents, that favours the corresponding NiO→gCN interfacial electron transfer, ultimately resulting in a better functional activity. These conclusions are also corroborated by the PL and XPS results, evidencing an enhanced interfacial charge transfer according to the sequence trend gCN/NiO NDL < gCN/NiO NDH < gCN/NiO UD, and by the Nyquist plots reported in Figure S19, that reveal a corresponding decrease of charge transfer resistance.

To attain a deeper insight into the obtained electrocatalytic activity trend, the flat band potential (E_{FB}) values, assumed to be coincident with the Fermi energy,[31] were estimated by the intercept of the square photocurrent density curves with the potential axis (see Figures 7d and S20). The obtained values, in excellent agreement with the above-discussed electrochemical results, further explain why gCN/NiO UD is the best performing electrocatalyst, since a deeper Fermi level energy enables to achieve the OER reaction onset with a lower electrode polarization.[10a] Conversely, for gCN/NiO NDH and gCN/NiO NDL, the application of a higher bias is necessary to obtain the same current density with respect to the gCN/NiO UD sample.

The results discussed so far, in conjunction with band gap values (see above) and the data obtained by XPS valence band analyses (Figure S21), enabled us to construct the scheme proposed in Figure 8. Upon irradiation, electron-hole pairs are generated both on gCN and NiO.[1e] The excited electrons in NiO CB are transferred to gCN CB and subsequently, thanks to the action of the applied electric field, to the counterelectrode, where hydrogen production takes place. In a different way, photogenerated holes flow from gCN VB to NiO CB. Accordingly, the separation of photogenerated charge carrier in gCN/NiO materials is enhanced, resulting thus in improved functional performances.

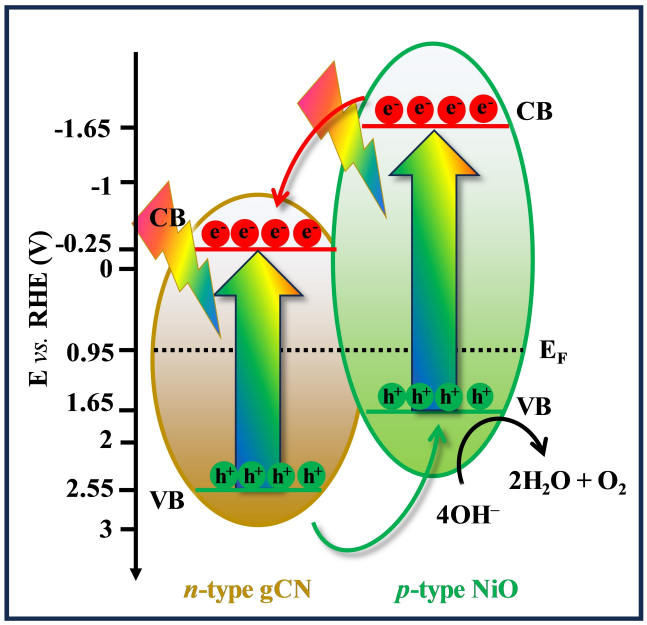

Figure 8. Interfacial band structure for the NiO/gCN heterojunction. Valence and conduction band edge positions (VB and CB, respectively) were obtained by photoelectron spectroscopy measurements and optical band gap values (Figure 2c, S2b and S21). The marked Fermi level energy (E_F) corresponds to specimen gCN/NiO UD. The mean band gap for gCN as reported in Figure 2c is 2.82 eV, while that of NiO is 3.3 eV.[8e,30] The scheme is valid for all the present gCN/NiO specimens, with the only difference in the Fermi level position and, consequently on the VB and CB edges (0.01 and 0.015 V for gCN/NiO NDH and NDL, respectively; these small shifts are not reported in the diagram).

As a proof-of-concept, and in view of possible practical applications, the best performing gCN/NiO UD electrocatalyst was also tested under illumination for OER in alkaline seawater (Figures 9 and S22), never reported so far for analogous systems. In spite of the corrosive reaction environment, the photocurrent density at 1.65 V *vs.* RHE did not undergo any appreciable decrease with respect to the 0.1 M KOH case (Table S5), and prolonged chronoamperometric tests highlighted a very good stability (compare insets of Figures 7a and 9a). Even in this case, Tafel slopes underwent an appreciable decrease under illumination (Figure 9c). Remarkably, the current densities for the present materials and the corresponding Tafel slopes (Tables S5–S6), especially those of the best performing samples, compare favourably with those reported up to date in various literature reports not only for similar electrocatalysts, but also for different benchmark systems based on IrO_2 and RuO_2 (see Tables S7 and S8). These results highlight the potential of the proposed fabrication strategy for the obtainment of efficient OER electrocatalysts and the amenable modulation of their performances as a function of NiO dispersion. This application prospect is further reinforced by the very good material service life, as assessed by the LSVs collected

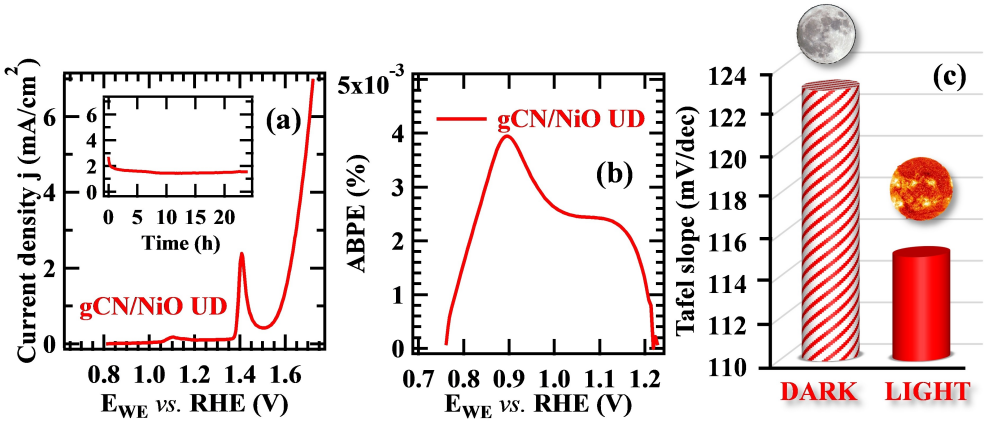

Figure 9. LSV curve registered under irradiation (a), ABPE% curve (b), and Tafel slopes (c) in the dark and under illumination for gCN/NiO UD. A prolonged CA curve registered at 1.6 V *vs.* RHE is shown as inset in panel (a). Data have been obtained utilizing as electrolyte Adriatic alkaline seawater (pH = 13.58).

every 90 days (Figure S23) for six months upon sample storage under ambient conditions. The system service life was also corroborated by *post operando* compositional and morphological analyses (Figures S24–S26), that enabled to exclude the occurrence of significant variations upon prolonged functional testing. Overall, these outcomes open intriguing perspectives for sustainable energy production from solar light and seawater, largely abundant and low-cost natural resources, without any ecological footprint.

Conclusions

In summary, this work proposes a straightforward preparation route to gCN nanoarchitectures integrating NiO as a co-catalyst for photo-activated oxygen evolution in water splitting. Specifically, the systems are grown on carbon cloth substrates by a single-step electrophoretic process, followed by a final thermal treatment in air. As elucidated by a multi-technique characterization, the proposed strategy enabled to obtain pure gCN nanostructures featuring an open morphology and an intimate contact with the hosted NiO. Interestingly, a proper control of preparative conditions enables to tailor nickel(II) oxide distribution in gCN, obtaining nano- or ultra-dispersed NiO. The high density of the formed NiO/gCN heterojunctions significantly promotes the separation of photogenerated charge carriers, yielding an improved OER photoactivity in comparison to the pristine gCN, especially in the latter case. The obtained gCN/NiO specimens are demonstrated as noble metal-free, cost-effective and efficient OER photoelectrocatalysts not only in alkaline freshwater, but even in seawater. These characteristics, along with the favorable durability, are of considerable interest for real-world sustainable energy generation from abundant and renewable natural resources.

Overall, this work may provide new insights and highlight promising prospects to use ultra-dispersed functional activators for the engineering of gCN-based materials, modulating the system chemico-physical properties and boosting the electrocatalytic performances. Due to the facile synthetic method and attractive activity, the target composites represent a valuable alternative to noble metal-based systems as low-cost and efficient catalysts for a variety of energy-related applications.

Experimental Section

Material Preparation

The synthesis of gCN powders has been performed following a previously reported literature procedure.[8j] The functionalization of the above described gCN powders with nickel oxide was performed after a modification of a previously proposed route.[2b] Depositions on CC substrates were performed from freshly prepared suspensions of gCN/NiO powders and I_2 in acetone at a constant potential difference of 10 V for 60 s. For comparison, bare NiO was also fabricated and characterized. All the pertaining details are available in the Supporting Information (§S1-1).

Material Characterization

FT-IR spectra were registered in the range 400–4000 cm^{-1} on a JASCO 4100 instrument equipped with a EasiDif accessory (PIKE Technologies, Inc.), using KBr as a reference, operating in diffuse reflectance mode. Optical absorption spectra were recorded operating in diffuse reflectance mode on a Varian Cary 50 dual-beam spectrophotometer (spectral bandwidth = 1 nm), using $BaSO_4$ substrate as a reference. The band gap (E_G) of gCN-containing samples was evaluated using the Tauc relation:[10b]

$$[f(R)h\nu]^n = K(h\nu - E_G) \quad (1)$$

where f(R) is the Kubelka-Munk function, R is the measured reflectance, hν is the photon energy, K is a constant, and $n = 1/2$ for indirect allowed transitions, reported to be the strongest ones for gCN,[32] the main system component. E_G values were obtained by extrapolating the straight portion of experimental curves to intersect the energy axis at $\alpha = 0$. FE-SEM and EDXS analyses were performed using a Zeiss SUPRA 40 VP apparatus equipped with an INCA x-act PentaFET Precision spectrometer, using primary electron beam voltages between 10 and 20 kV. The mean particle sizes were evaluated using the ImageJ® software. XPS analyses were carried out at an operating pressure of 5×10^{-9} mbar, using a ThermoFisher

Scientific ESCALAB™ QXi instrument equipped with a monochromatized AlKα excitation source (hν = 1486.6 eV), funded by "Sviluppo delle infrastrutture e programma biennale degli interventi del Consiglio Nazionale delle Ricerche (2019)". Survey spectra were collected in the binding energy (BE) range 0–1300 eV, using the following parameters: 150 eV pass energy; 1.0 eV/step; 0.05 s/step. High resolution spectra were obtained collecting data at 50 eV pass energy, 0.05 eV/step and 0.05 s/step. BE values (uncertainty = ± 0.1 eV) were corrected for charging by assigning a position of 284.8 eV to the adventitious C1s signal (C_0 in Figure 3a and S5).[33] Peak fitting was performed using the XPSPeak software and applying a Shirley-type background subtraction. Atomic percentages (at.%) were evaluated by peak area integration, using sensitivity factors supplied by ThermoFisher. TEM analyses, including BF-HRTEM, HAADF-STEM, SAED, and EDXS analyses were carried out using a JEOL ARM200 F cold FEG double-aberration corrected microscope equipped with a large-angle CENTURIO EDX detector, an ORIUS Gatan camera, and Quantum GIF, operating at 200 kV.

Electrochemical Tests

Photoelectrocatalytic activity tests were performed at room temperature in 0.1 M KOH aqueous solution (pH = 13.05) by an integrated system consisting of a Zennium-PRO and a PP212 unit from Zahner GmbH, coupled with an optical bench containing a Zahner photoelectrochemical cell. Carbon cloth-supported gCN/NiO systems were used as working electrodes, whereas a Pt coil and an Ag/AgCl electrode ($E^{\circ}_{Ag/AgCl} = 0.199$ V) were used as counter- and reference electrode, respectively. To prevent wetting of the electrical contact by the electrolyte due to capillary phenomena, a nickel-coated copper wire was carefully glued on the edge of the carbon cloth, and the substrate-wire contact was subsequently coated with epoxy resin. Tafel slopes were determined by analyzing the plots of potential *vs.* log(current density). LSV measurements (scan rate = 5 mV/s) were performed in freshwater containing 0.1 M KOH and, for the best-performing sample, even in Adriatic seawater picked up at the seaside of Rosolina (RO), Italy. This was preliminarily treated adding KOH and filtering the precipitate [mainly formed by $Mg(OH)_2$; final pH = 13.58]. ABPE curves were obtained through the equation:[2c,5d]

$$\text{ABPE}\ (\%) = ([j \times (1.23 - E)]/P) \times 100 \quad (2)$$

where j (mA/cm^2) is the photocurrent density at the potential E (V *vs.* RHE) and P is the incident light intensity (50 mW/cm^2, emitted from a white LED source), constantly measured by a photodiode in front of the cell. Chronoamperometry (CA) analyses were carried out at 1.65 V (*vs.* RHE). Further information on material characterization and functional test can be found in the Supporting Information.

Acknowledgements

This research was financially supported by the National Council of Research (Progetti di Ricerca @CNR-avviso 2020-ASSIST), Padova University (P-DiSC#04BIRD2020-UNIPD EUREKA, P-DiSC#02BIRD2023-UNIPD RIGENERA, DOR 2021–2023), INSTM Consortium (INSTM21PDGASPAROTTO-NANO^{MAT}, INSTM21 PDBARMAC-ATENA), and PRIN 2022474YE8 (SCI-TROPHY project). Open Access publishing facilitated by Consiglio Nazionale delle Ricerche, as part of the Wiley - CRUI-CARE agreement.

Conflict of Interests

There are no conflicts to declare.

Data Availability Statement

The data that support the findings of this study are available from the corresponding author upon reasonable request.

Keywords: NiO · graphitic carbon nitride · nanostructures · electrophoretic deposition · oxygen evolution reaction

[1] a) Y. Liu, D. Zhou, T. Deng, G. He, A. Chen, X. Sun, Y. Yang, P. Miao, *ChemSusChem* **2021**, *14*, 5359–5383; b) H. Yang, H. Guo, K. Pang, P. Fan, X. Li, W. Ren, R. Song, *Nanoscale* **2020**, *12*, 7024–7034; c) T. Ma, J. Bai, C. Li, *Vacuum* **2017**, *145*, 47–54; d) W. Wang, B. Lv, F. Tao, *Environ. Sci. Pollut. Res. Int.* **2023**, *30*, 25620–25634; e) L. Wang, Y. Dong, J. Zhang, F. Tao, J. Xu, *J. Solid State Chem.* **2022**, *308*, 122878; f) L. Wang, W. Si, Y. Tong, F. Hou, D. Pergolesi, J. Hou, T. Lippert, S. X. Dou, J. Liang, *Carbon Energy* **2020**, *2*, 223–250; g) C. Han, R. Zhang, Y. Ye, L. Wang, Z. Ma, F. Su, H. Xie, Y. Zhou, P. K. Wong, L. Ye, *J. Mater. Chem. A* **2019**, *7*, 9726–9735; h) L. Wang, Y. Li, X. Yin, Y. Wang, A. Song, Z. Ma, X. Qin, G. Shao, *ACS Sustainable Chem. Eng.* **2017**, *5*, 7993–8003; i) X. Li, H. Zhang, Y. Liu, X. Duan, X. Xu, S. Liu, H. Sun, S. Wang, *Chem. Eng. J.* **2020**, *390*, 124634.

[2] a) T. u Haq, Y. Haik, *ACS Sustainable Chem. Eng.* **2022**, *10*, 6622–6632; b) M. I. Chebanenko, A. A. Lobinsky, V. N. Nevedomskiy, V. I. Popkov, *Dalton Trans.* **2020**, *49*, 12088–12097; c) M. Benedet, G. A. Rizzi, A. Gasparotto, N. Gauquelin, A. Orekhov, J. Verbeeck, C. Maccato, D. Barreca, *Appl. Surf. Sci.* **2023**, *618*, 156652; d) D. Guo, Z. Zhao, M.-Y. Zong, C. Fan, W. Zheng, D. Wang, *ACS Sustainable Chem. Eng.* **2023**, *11*, 8362–8373; e) M. Tang, T. Yang, X. Wang, J. Ge, *J. Phys. Chem. C* **2024**, *128*, 1547–1561.

[3] C. Liu, J. Liu, R. Godin, *ACS Catal.* **2023**, *13*, 573–586.

[4] a) K. Hemmati, A. Kumar, A. R. Jadhav, O. Moradlou, A. Z. Moshfegh, H. Lee, *ACS Catal.* **2023**, *13*, 5516–5528; b) S. Noor, R. S. Haider, S. Noor, S. Sajjad, S. A. Khan Leghari, M. Mehboob, M. Long, *Int. J. Hydrogen Energy* **2022**, *47*, 36517–36529; c) S. Zhang, J. Yan, S. Yang, Y. Xu, X. Cai, X. Li, X. Zhang, F. Peng, Y. Fang, *Chin. J. Catal.* **2017**, *38*, 365–371; d) M. Tahir, L. Pan, F. Idrees, X. Zhang, L. Wang, J.-J. Zou, Z. L. Wang, *Nano Energy* **2017**, *37*, 136–157; e) Y. Dong, Y. Chen, P. Jiang, G. Wang, X. Wu, R. Wu, *RSC Adv.* **2016**, *6*, 7465–7473; f) W. Zhang, J. Albero, L. Xi, K. M. Lange, H. Garcia, X. Wang, M. Shalom, *ACS Appl. Mater. Interfaces* **2017**, *9*, 32667–32677; g) S. F. Blaskievicz, H. L. S. Santos, I. F. Teixeira, J. L. Bott-Neto, P. S. Fernández, L. H. Mascaro, *Mater. Today Nano* **2022**, *18*, 100192; h) P. Longchin, D. Mitoraj, O. M. Reyes, C. Adler, N. Wetchakun, R. Beranek, *J. Phys. E* **2020**, *2*, 044001.

[5] a) K. Bhunia, S. Khilari, M. Chandra, D. Pradhan, S.-J. Kim, *J. Alloys Compd.* **2023**, *935*, 167842; b) X. Li, P. Cui, W. Zhong, J. Li, X. Wang, Z. Wang, J. Jiang, *Chem. Commun.* **2016**, *52*, 13233–13236; c) C. Liao, B. Yang, N. Zhang, M. Liu, G. Chen, X. Jiang, G. Chen, J. Yang, X. Liu, T.-S. Chan, Y.-J. Lu, R. Ma, W. Zhou, *Adv. Funct. Mater.* **2019**, *29*, 1904020; d) M. Benedet, G. A. Rizzi, O. I. Lebedev, V. Roddatis, C. Sada, J.-L. Wree, A. Devi, C. Maccato, A. Gasparotto, D. Barreca, *J. Mater. Chem. A* **2023**, *11*, 21595–21609; e) M. Benedet, G. A. Rizzi, D. Barreca, A. Gasparotto, C. Maccato, *Surf. Sci. Spectra* **2023**, *30*, 014004; f) M. Benedet, A. Gasparotto, G. A. Rizzi, C. Maccato, D. Mariotti, R. McGlynn, D. Barreca, *Surf. Sci. Spectra* **2023**, *30*, 024018; g) N.-T. Suen, S.-F. Hung, Q. Quan, N. Zhang, Y.-J. Xu, H. M. Chen, *Chem. Soc. Rev.* **2017**, *46*, 337–365; h) A. Naderi, M. Jourshabani, B.-K. Lee, *ACS Sustainable Chem. Eng.* **2023**, *11*, 9010–9019; i) J. Tian, Q. Liu, A. M. Asiri, K. A. Alamry, X. Sun, *ChemSusChem* **2014**, *7*, 2125–2130.

[6] a) R. Wang, K. Pan, D. Han, J. Jiang, C. Xiang, Z. Huang, L. Zhang, X. Xiang, *ChemSusChem* **2016**, *9*, 2470–2479; b) V. D. Silva, T. A. Simões, J. P. F. Grilo, E. S. Medeiros, D. A. Macedo, *J. Mater. Sci.* **2020**, *55*, 6648–6659.

[7] P. Chaudhary, P. P. Ingole, *Int. J. Hydrogen Energy* **2020**, *45*, 16060–16070.

[8] a) S. K. Lakhera, R. T. Pangal, H. Y. Hafeez, B. Neppolian, *ChemSusChem* **2019**, *12*, 4293–4303; b) J. Liu, Q. Jia, J. Long, X. Wang, Z. Gao, Q. Gu,

Appl. Catal. B **2018**, *222*, 35–43; c) Y. Fu, C. a Liu, C. Zhu, H. Wang, Y. Dou, W. Shi, M. Shao, H. Huang, Y. Liu, Z. Kang, *Inorg. Chem. Front.* **2018**, *5*, 1646–1652; d) P. Qiu, C. Xu, H. Chen, F. Jiang, X. Wang, R. Lu, X. Zhang, *Appl. Catal. B* **2017**, *206*, 319–327; e) T. Zhang, P. Liu, L. Wang, S. Wang, J. Shi, X. Lan, *Materials* **2021**, *14*, 2894; f) J.-y. Tang, R.-t. Guo, W.-g. Zhou, C.-y. Huang, W.-g. Pan, *Appl. Catal. B* **2018**, *237*, 802–810; g) X. Bai, T. Jia, D. Hao, Y. Xin, L. Guo, *CrystEngComm* **2022**, *24*, 2023–2035; h) M. Benedet, A. Gasparotto, G. A. Rizzi, D. Barreca, C. Maccato, *Surf. Sci. Spectra* **2022**, *29*, 024001; i) M. Benedet, D. Barreca, G. A. Rizzi, C. Maccato, J.-L. Wree, A. Devi, A. Gasparotto, *Surf. Sci. Spectra* **2023**, *30*, 024021; j) Y.-S. Jun, E. Z. Lee, X. Wang, W. H. Hong, G. D. Stucky, A. Thomas, *Adv. Funct. Mater.* **2013**, *23*, 3661–3667; k) L. Lei, W. Wang, C. Wang, M. Zhang, Q. Zhong, H. Fan, *Ceram. Int.* **2021**, *47*, 1258–1267.

[9] a) Y. Li, Y. Wang, C.-L. Dong, Y.-C. Huang, J. Chen, Z. Zhang, F. Meng, Q. Zhang, Y. Huangfu, D. Zhao, L. Gu, S. Shen, *Chem. Sci.* **2021**, *12*, 3633–3643; b) G. Tzvetkov, M. Tsvetkov, T. Spassov, *Superlattices Microstruct.* **2018**, *119*, 122–133; c) Z. Zhao, Y. Sun, F. Dong, *Nanoscale* **2015**, *7*, 15–37.

[10] a) M. Benedet, A. Gallo, C. Maccato, G. A. Rizzi, D. Barreca, O. I. Lebedev, E. Modin, R. McGlynn, D. Mariotti, A. Gasparotto, *ACS Appl. Mater. Interfaces* **2023**, *15*, 47368–47380; b) M. Benedet, G. A. Rizzi, A. Gasparotto, O. I. Lebedev, L. Girardi, C. Maccato, D. Barreca, *Chem. Eng. J.* **2022**, *448*, 137645; c) S. Benedoue, M. Benedet, A. Gasparotto, N. Gauquelin, A. Orekhov, J. Verbeeck, R. Seraglia, G. Pagot, G. A. Rizzi, V. Balzano, L. Gavioli, V. D. Noto, D. Barreca, C. Maccato, *Nanomaterials* **2023**, *13*, 1035; d) X. Li, Y. Yang, B. Yue, J. Lin, Q. Hu, P. Li, Y. Liu, L. Duan, Q. Zhuang, Y. Wang, J. Liu, *Electrochim. Acta* **2023**, *466*, 143056.

[11] a) Y. Wang, X. Li, R. Zhao, N. Zhang, B. Zhu, J. Yang, *Appl. Surf. Sci.* **2020**, *532*, 147410; b) P. Deng, W. Hong, Z. Cheng, L. Zhang, Y. Hou, *Int. J. Hydrogen Energy* **2020**, *45*, 33543–33551; c) G. Zhang, G. Li, X. Wang, *ChemCatChem* **2015**, *7*, 2864–2870; d) S. Ohn, S. Y. Kim, S. K. Mun, J. Oh, Y. J. Sa, S. Park, S. H. Joo, S. J. Kwon, S. Park, *Carbon* **2017**, *124*, 180–187.

[12] K. Qi, A. Zada, Y. Yang, Q. Chen, A. Khataee, *Res. Chem. Intermed.* **2020**, *46*, 5281–5295.

[13] a) M. A. Peck, M. A. Langell, *Chem. Mater.* **2012**, *24*, 4483–4490; b) X. Li, Y. Wang, W. Tian, J. Cao, *ACS Omega* **2019**, *4*, 9645–9653; c) N. Wen, D. Zhang, X. Zhao, X. Jiao, Y. Xia, D. Chen, *ACS Catal.* **2023**, *13*, 7868–7878.

[14] I. S. Pieta, A. Rathi, P. Pieta, R. Nowakowski, M. Hołdynski, M. Pisarek, A. Kaminska, M. B. Gawande, R. Zboril, *Appl. Catal. B* **2019**, *244*, 272–283.

[15] N. Cheng, L. Zhang, K. Doyle-Davis, X. Sun, *Electrochem. Energy Rev.* **2019**, *2*, 539–573.

[16] a) J. Zhu, L. Kong, X. Shen, G. Zhu, Z. Ji, K. Xu, H. Zhou, X. Yue, B. Li, *J. Electroanal. Chem.* **2020**, *873*, 114390; b) L. Lei, H. Fan, Y. Jia, X. Wu, Q. Zhong, W. Wang, *Appl. Surf. Sci.* **2022**, *606*, 154938.

[17] D. Barreca, G. Carraro, A. Gasparotto, C. Maccato, M. E. A. Warwick, K. Kaunisto, C. Sada, S. Turner, Y. Gönüllü, T.-P. Ruoko, L. Borgese, E. Bontempi, G. Van Tendeloo, H. Lemmetyinen, S. Mathur, *Adv. Mater. Interfaces* **2015**, *2*, 1500313.

[18] N. D. Shcherban, P. Mäki-Arvela, A. Aho, S. A. Sergiienko, P. S. Yaremov, K. Eränen, D. Y. Murzin, *Catal. Sci. Technol.* **2018**, *8*, 2928–2937.

[19] J. Bian, Q. Li, C. Huang, J. Li, Y. Guo, M. Zaw, R.-Q. Zhang, *Nano Energy* **2015**, *15*, 353–361.

[20] a) S. Panimalar, R. Uthrakumar, E. T. Selvi, P. Gomathy, C. Inmozhi, K. Kaviyarasu, J. Kennedy, *Surf. Interfaces* **2020**, *20*, 100512; b) Y. Zhang, Q. Pan, G. Chai, M. Liang, G. Dong, Q. Zhang, J. Qiu, *Sci. Rep.* **2013**, *3*, 1943.

[21] S. Arshad, M. Imran, A. Haider, A. Shahzadi, H. Saeed, A. Ul-Hamid, M. M. Al-Anazy, E. S. Yousef, M. Ikram, *J. Inorg. Organomet. Polym. Mater.* **2023**.

[22] I. Bertóti, M. Mohai, K. László, *Carbon* **2015**, *84*, 185–196.

[23] P. Qiu, H. Chen, F. Jiang, *RSC Adv.* **2014**, *4*, 39969–39977.

[24] Y. Xiao, G. Tian, W. Li, Y. Xie, B. Jiang, C. Tian, D. Zhao, H. Fu, *J. Am. Chem. Soc.* **2019**, *141*, 2508–2515.

[25] a) I. Preda, R. J. O. Mossanek, M. Abbate, L. Alvarez, J. Méndez, A. Gutiérrez, L. Soriano, *Surf. Sci.* **2012**, *606*, 1426–1430; b) G. Pagot, M. Benedet, C. Maccato, D. Barreca, V. Di Noto, *Surf. Sci. Spectra* **2023**, *30*, 024028.

[26] a) J. F. Moulder, W. F. Stickle, P. E. Sobol, K. D. Bomben, *Handbook of X-ray Photoelectron Spectroscopy*, Perkin Elmer Corporation, Eden Prairie, MN, USA, **1992**; b) http://srdata.nist.gov/xps.

[27] O. Pérez, O. F. Odio, E. Reguera, *New J. Chem.* **2022**, *46*, 11255–11265.

[28] ICSD card N° 9866.

[29] a) Š. Trafela, J. Zavašnik, S. Šturm, K. Ž. Rožman, *Electrochim. Acta* **2019**, *309*, 346–353; b) M. Alsabet, M. Grdeń, G. Jerkiewicz, *Electrocatalysis* **2015**, *6*, 60–71.

[30] M. Benedet, C. Maccato, G. Pagot, C. Invernizzi, C. Sada, V. Di Noto, G. A. Rizzi, E. Fois, G. Tabacchi, D. Barreca, *J. Phys. Chem. C* **2023**, *127*, 22304–22314.

[31] H. Li, H. Yu, X. Quan, S. Chen, Y. Zhang, *ACS Appl. Mater. Interfaces* **2016**, *8*, 2111–2119.

[32] a) G. Liao, Y. Gong, L. Zhang, H. Gao, G.-J. Yang, B. Fang, *Energy Environ. Sci.* **2019**, *12*, 2080–2147; b) X. Wang, S. Blechert, M. Antonietti, *ACS Catal.* **2012**, *2*, 1596–1606.

[33] D. Briggs, M. P. Seah, *Practical Surface Analysis: Auger and X-ray Photoelectron Spectroscopy*, 2nd ed., Wiley, New York, **1990**.

Manuscript received: May 3, 2024
Revised manuscript received: June 12, 2024
Version of record online: July 9, 2024